Pitting behavior of friction stir repair-welded 304L stainless steel in 3.5% NaCl solution at room temperature: role of grain and defect structures

Anirban Naskar[1] · Madhumanti Bhattacharyya[1] · Krishnan S. Raja[1] · Indrajit Charit[1] · Jens Darsell[2] · Saumyadeep Jana[2]

Abstract

Stainless steel (SS) canisters used for storing spent nuclear waste are prone to chloride-induced stress corrosion cracking. Friction stir welding (FSW), being a low heat input process, can be used for repair welding of these canisters. In this study, an artificial crack was introduced on the 304L SS coupons by an electric discharge machining process. The artificial crack was repair-welded by FSW by maintaining the tool temperature a constant at two levels (725 and 825 °C). Friction stirring significantly reduced the grain size of the stirred zone (SZ) from about 47 to 2–4 μm. The fraction of low-angle grain boundaries increased in the SZ from 2 to 37–43%. On the other hand, the fraction of special grain boundaries (Σ3 and Σ9) that was ~ 50% in the base metal reduced to < 10% in the SZ. During friction stirring, the oxide layer of artificial crack was broken and aligned to form a spiral defect called lazy-S structure. All these microstructural changes affected the corrosion behavior of the FSW specimens when tested in 3.5% NaCl at room temperature using cyclic polarization, chronoamperometry, and electrochemical impedance spectroscopy. The FSW specimens showed lower polarization resistance and lower transpassive potential than those of the base metal specimens. However, the pitting protection potentials of the FSW specimens were higher than that of the base metal. The pitting behavior of the FSW specimens was influenced more by the preferential attack on the lazy-S region than by passive film breakdown. The flat band potentials of the passive film formed on the FSW specimens were more positive than that of base metal. The charge carrier density of passive film formed on the FSW specimens was higher than that of the base metal. The higher fraction of low-angle grain boundaries present in the FSW specimens could supply more number of misorientation dislocations at the metal/film interface which could form anion vacancies by a climb process leading to formation of oxide at these locations without stressing the substrate. Therefore, low-angle boundaries are considered helpful for formation of stress-free passive films that will be highly stable and enhance both pitting and stress corrosion cracking resistance.

Keywords Dry storage canister · Stress corrosion cracking (SCC) · Pitting corrosion · Friction stirwelding (FSW) · Lazy-S · Low angle grain boundaries

1 Introduction

Effective handling of radioactive nuclear wastes is a major concern. Dry storage systems have been widely adopted for long-term storage of used nuclear fuels that consist of several stainless steel (SS) canisters [1–3]. Typically, 304L or 316-type austenitic stainless steels plates are fusion-welded together to fabricate the storage canisters. Even though these canisters provide a safer way of storing the used nuclear fuels, an underlying problem of

✉ Krishnan S. Raja, ksraja@uidaho.edu | [1]Chemical and Materials Engineering, University of Idaho, Moscow, ID 83844-1021, USA. [2]Pacific Northwest National Laboratory, 902 Battelle Blvd, Richland, WA 99354, USA.

chloride-induced stress corrosion cracking (SCC) of stainless steel canisters remains to be solved. Salts carried by the dust in the atmosphere may settle on the canisters and subsequently deliquesce as heat generated by radioactive decay declines over time. The deliquescence of salt deposit could induce various forms of corrosion attack, such as pitting and CISCC [4, 5]. Pitting corrosion occurs in austenitic SS readily in the presence of chloride solution [6]. The chloride-induced pits that are formed on austenitic SS can act as stress concentrators and further facilitate SCC [4]. Pitting in austenitic stainless steels and their weldments is influenced by various metallurgical factors. The microstructural features such as grain boundaries [7], grain size [8], presence of second-phase particles and inclusions like carbides or manganese sulfide (MnS) [9] can act as pit nucleation sites in austenitic stainless steel. Further, external factors such as the composition of chloride-containing electrolyte [10] and surface finish [11] influence the pitting tendencies in stainless steels. Chloride-induced pitting and stress corrosion cracking are the potential failure mechanisms of stainless steel canisters. Repair welding of SCC cracks is one of the strategies to expand the life span of the stainless steel canisters [12]. The problems with the fusion welding (such as chromium depletion and grain growth at the heat-affected zone (HAZ), segregation at the interdendrites) have been addressed by implementing a low heat input laser welding [13].

A solid-state friction stir welding (FSW) process for crack repair has been reported and showed promising results on the corrosion resistance of the crack-healed region [14]. However, another study showed that friction stir crack-repaired 304L specimens developed stress corrosion cracks on the weld nugget and along the advancing side of the weld when exposed to boiling magnesium chloride (155 °C) for 3 h [15]. On the other hand, friction stir-welded 316L SS showed a more noble pitting potential for the stirred zone than that of the base metal [16]. The increased corrosion resistance of the friction-stirred stainless steel weld nugget or stirred zone (SZ) was attributed to several factors such as: (a) finer grains developed due to severe plastic deformation that promote short-circuit diffusion of passive film-forming elements [17], (b) low-angle grain boundaries (2°–15°) [18–20], and (c) decreased donor density of passive films formed on the stirred zone [21]. Several investigators reported localized corrosion of friction stir-welded austenitic stainless steels (not necessarily 304 or 316 types), and the corrosion was attributed to features such as: (i) formation of delta ferrite in the SZ of nickel-free austenitic stainless steel and subsequent enrichment of ferrite-stabilizing elements in the delta ferrite that lead to localized depletion of Cr at the austenite/ferrite interface [22], (ii) tool wear debris that caused galvanic effect [23], (iii) formation of topologically close-packed (TCP) phases

such as σ and χ [24], and (iv) high reactivity of the stirred zone or thermomechanically affected zone (TMAZ) due to a high defect density that rendered the passive film to be less protective [25].

The review of recent literature on the corrosion behavior of the friction stir-welded stainless steel materials showed both positive and negative attributes. This work focuses on the friction stir repair of an existing crack and the influence of repair welding on the corrosion behavior. To this effect, an artificial crack was introduced by the electric discharge machining (EDM), a narrow slit at the center of 304L SS coupons. The simulated EDM crack on the 304L SS coupon was repaired or healed by FSW by maintaining two different isothermal tool temperatures such as 725 and 825 °C. The electrochemical corrosion behavior of the friction stir repair-welded 304L specimens was investigated using cyclic and potentiostatic polarization and electrochemical impedance spectroscopic techniques in 3.5% NaCl solution (pH unadjusted) and compared with that of unaffected base metal specimens.

2 Experimental

2.1 Material and repair welding

Simulated cracks were introduced at the centre of the 304L coupons (330 mm (L) × 149 mm (W) × 12.7 mm (T)) by creating slots (5 mm deep and 0.33 mm wide) using EDM along the length of the plates, as illustrated in Fig. 1. Single-pass FSW was performed on plates to repair the simulated cracks at the Pacific Northwest National Laboratory (PNNL) using a gantry-type TTI FSW machine. A polycrystalline cubic boron nitride (PCBN) tool (MegaStir™) with a
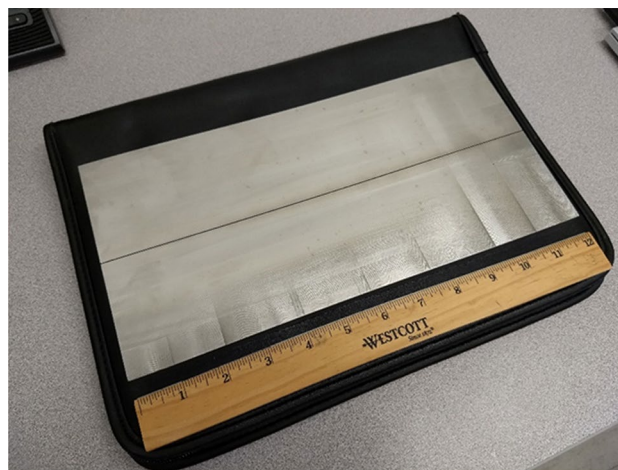

Fig. 1 Image of the 304L stainless steel coupon with a simulated crack introduced by electric discharge machining

shoulder diameter of 36.8 mm and pin length of 5.7 mm was used for the FSW. The tool tilt angle was − 0.5°. The FSW was carried out at isothermal conditions by keeping the tool temperature constant at either 725 or 825 °C. The welding speed was 25.4 mm/s in both the temperatures. The welds were carried out in power-controlled mode. The tool speed changes continuously through the length of the weld to maintain a steady power and thus a steady temperature. A customized algorithm that was developed at PNNL was used for both FSW runs. The specialty of this algorithm is that it can maintain a desired weld temperature during the course of FSW tool travel. Fixed weld temperatures were achieved through varying the angular velocity of FSW tool using a feedback mechanism, at a user-specified weld power. PNNL has worked extensively in developing and fine-tuning the control parameters (proportional–integral–derivative PID constants) to ensure a steady weld temperature. (Maximum diversion was noted to be < 1 °C from the specified weld temperature.) Table 1 summarizes the welding parameters employed in this study. The welding parameters (such as rotational speed, vertical forging load, and spindle torque) were selected by the machine algorithm based on the specified welding power, isothermal condition, and linear welding speed. The welding speed was kept at 25.4 mm/min to maintain the lateral load on the PCBN tool in the acceptable range. Higher lateral load can cause premature tool failure.

2.2 Microstructural characterization

Small specimens were cut from the FSW coupons and metallographically polished down to 0.05 μm alumina slurry using a vibratory polisher for 10 h (Pace Technologies GIGA-900). The mirror-finished samples were electrochemically etched using a 10 wt% oxalic acid aqueous solution. The etching was performed at 10 V for 20 s. Electron backscattered diffraction (EBSD) was performed in a JEOL JSL-6610LV SEM equipped with Hikari camera and TSL OIM v6 data collection software with 20 V accelerating voltage, 70° tilt, and 0.1 μm step size. This was to determine the average grain size in the stir zone and to map grain boundaries as well as misorientation. Grain size

measurement was done using the mean linear intercept (MLI) method for all the samples.

2.3 Corrosion studies

The FSW 304L SS samples were cut down to a size of 1 cm^2 and metallographically polished down to 1 μm finish. Corrosion characterizations were performed using a three-electrode setup and a potentiostat. A spiral Pt-wire of area 2 cm^2 and an Ag/AgCl in saturated KCl electrode (− 46 mV Vs. SCE) were used as counter and reference electrodes. A 3.5% NaCl (0.6 M) solution is used as an electrolyte for the tests. No aeration or deaeration of electrolyte was carried out. In the beginning, the samples were dipped in the electrolyte in an open-circuit condition until steady-state corrosion potential (OCP) was achieved. After reaching the OCP, linear polarization tests were carried out by scanning the potential in the range of ± 25 mV with respect to the OCP and at a 0.5 mV/s scan rate. Electrochemical impedance spectroscopy (EIS) tests were carried out on the samples at the OCP by varying the frequency from 10 kHz to 0.01 Hz. After EIS, cyclic polarization (CP) tests were performed in order to understand the pitting behavior. In the cyclic polarization, a forward potential scan was applied starting − 200 mV below the OCP at a scan rate 0.167 mV/s. The forward potential scan was reversed with a same scan rate when the apex current reached a current density of ~ 5 mA/cm^2. After polarization studies, the samples were then thoroughly cleaned by ultrasonication in deionized water. Potentiostatic tests were performed on the freshly polished specimens at a potential of 0 V Ag/AgCl. During the potentiostatic conditioning, a current decay behavior was observed initially when a stable passive film was stable. An increase in the current with time signified passivity breakdown. The potentiostatic tests were continued until a current density of 200 μA/cm^2 was reached. EIS was carried out at the beginning of the potentiostatic conditioning at 0 VAg/AgCl (referred to as pre-potentiostatic EIS), when a current density of > 20 μA/cm^2 was reached (this condition is referred to as pit initiation), and at the end of potentiostatic test when the current density exceeded 200 μA/cm^2 (referred to as pit growth). Mott–Schottky analysis was also carried out immediately after EIS. The Mott–Schottky analysis consisted of scanning the potential at 50 mV steps at every 2 s from 0 $V_{Ag/AgCl}$ in the cathodic direction to the initial OCPS value and measuring the imaginary impedance at 1000 Hz. Samples were observed under optical microscope before and after the potentiostatic runs.

Table 1 Friction stir welding parameters for isothermal tool temperature

Isothermal tool temperature (°C)	Welding speed (mm/min)	Tool rotational speed (rev/min)	Vertical forging load (kN)	Spindle torque (N.m)	Weld power (kW)
725	25.4	63–69	48.9	215.5	1.6
825	25.4	95–130	51.1	199.3	2.00
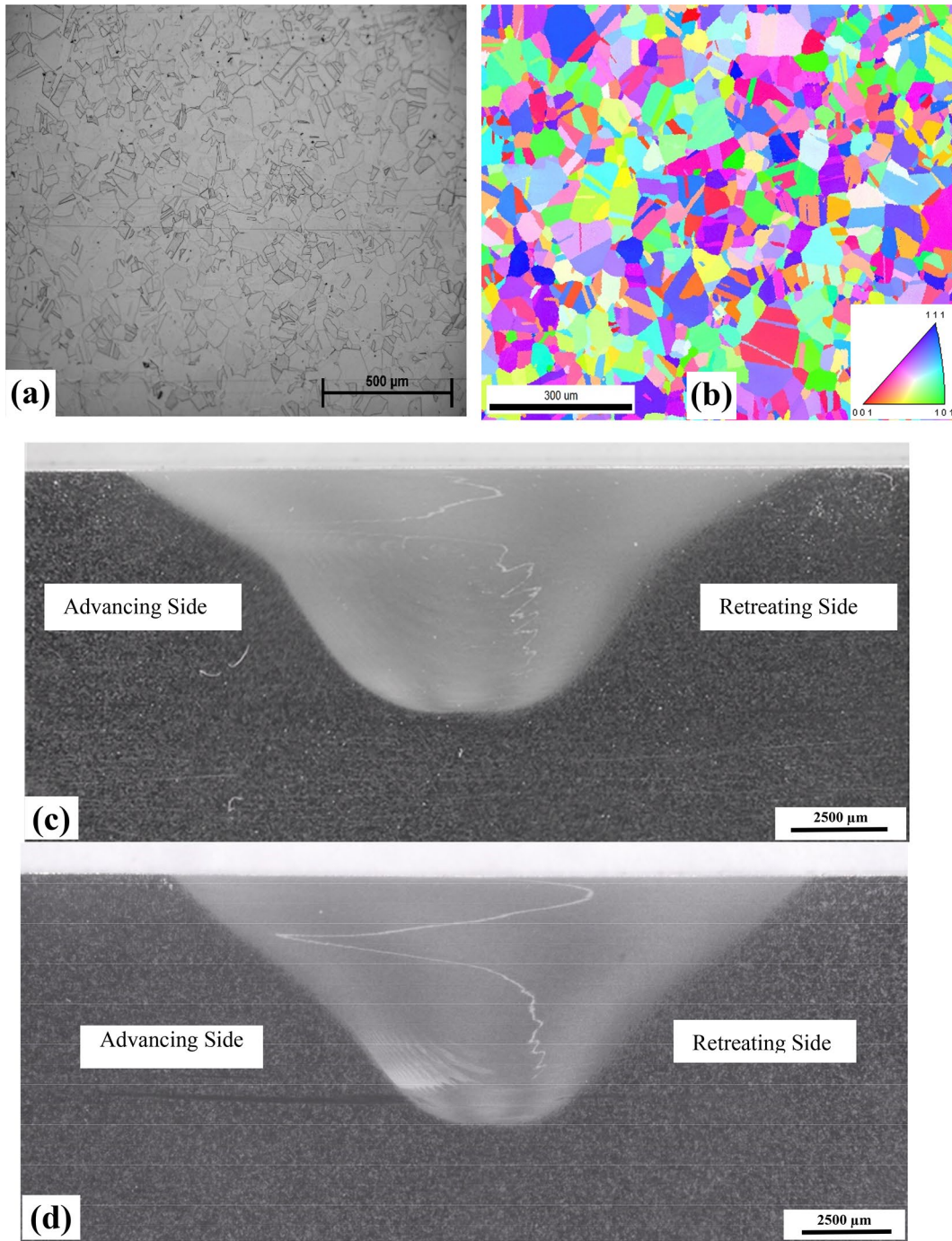
Fig. 2 Microstructures of 304L SS specimens: **a** optical microstructure of base metal (BM), **b** inverse pole figure (IPF) map of the as-received 304L SS BM from electron backscattered diffraction (EBSD) analysis; **c** friction stir welded at 725 °C and **d** friction stir welded at 825 °C

3 Results

3.1 Microstructures

The microstructure of the base metal (BM) is shown in Fig. 2. The optical microstructure in Fig. 2a shows equi-axed grains. The average grain size determined by the mean linear intercept method was 47 ± 16 μm as summarized in Table 1. Numerous annealing twins inside the grains are evident from the inverse pole figure map shown in Fig. 2b. A grain boundary mapping of the BM showed the presence of about 50% special boundary mostly in the form of Σ3 annealing twins. The fraction of low-angle grain

boundaries was very small. The fraction of random grain boundaries could be considered as 47.4%.

Figure 2c and d shows the shape of the stirred zones (SZ) welded in two different isothermal conditions such as 725 and 825 °C, respectively. The presence of spiral defects is evident in both the microstructures which is commonly known as 'lazy-S.' This lazy-S feature extends throughout the stir zone spanning the crown of the nugget and passing the root of the weld. This feature appears as an interface between the advancing and retreating sides that intermixed during the stirring operation [26, 27]. The lazy-S appeared because of breaking of the oxide layers which was initially formed on the artificial crack surfaces during the EDM process. A quick preliminary analysis using X-ray energy dispersion spectroscopy (EDS) of the lazy-S showed the presence of Cr-rich carbide and oxide particles. (Results are not shown here.) The number of curved interfaces in the bottom branch was more in the 725 °C sample as compared to the 825 °C one as shown in Fig. 2c and d. These lazy-S interface arcs were observed to be merging with the onion rings predominantly in the 725 °C sample. The presence of flow lines known as 'onion rings' could be observed at higher magnifications. The onion rings were predominantly found in the lower part of the SZ where material flow was influenced by the rotation of the pin. The ring spacing decreased as one moves away from the center toward the TMAZ interface. Formation of onion rings was explained by many researchers [28–30]. Disappearance of onion rings with increased tool rotation speed has also been reported in some previous studies [30]. The absence of onion rings in the top half of the SZ in both the samples can be attributed to intense material mixing driven by tool shoulder rotation [29].

Table 2 Summary of grain structure analyses of base metal and friction-stirred zone (SZ) of 304L SS from the EBSD data. Low-angle (2°–15°) grain boundaries are denoted as LAGB. The balance is % of random boundaries

| Location	Mean grain size (µm)	LAGB (2°–15°) (%)	Σ3 (%)	Σ9 (%)
Base metal	47 ± 16	2.2	47.7	2.7
725 °C SZ—top	2.4 ± 0.9	43.3	7.3	0.5
825 °C SZ—top	4.2 ± 1.4	37.3	9	0.6

Figure 3a and b shows inverse pole figure (IPF) maps of the SZ of FSWed samples at 725 and 825 °C, respectively. In both the FSW conditions, the SZ showed significant refinement in grain size as compared to BM. The grain boundary character distribution was different in the SZ compared to that of BM as summarized in Table 2. The fraction of low-angle grain boundary (LAGB) increased by an order of magnitude after severe plastic deformation during the FSW. This is attributed to the stirring process at 725 °C which has left some unrecrystallized part in the form of substructure. A decrease in the fraction of Σ3 and Σ9 fraction has also been noticed in the SZ as compared to that of BM. The severe plastic deformation could cause disappearance of the coincident lattice points in the boundary plane. Furthermore, migration of high-angle boundary (HAGB) during recrystallization could have resulted in a sharp drop in the number of annealing twins in the SZ. A marginal decrease in Σ3 fraction has also been noted on the SZ-advancing side which is mostly because of higher deformation associated with that side as compared to the retreating side [31]. The 825 °C SZ showed higher mean grain size than the 725 °C SZ which could be associated
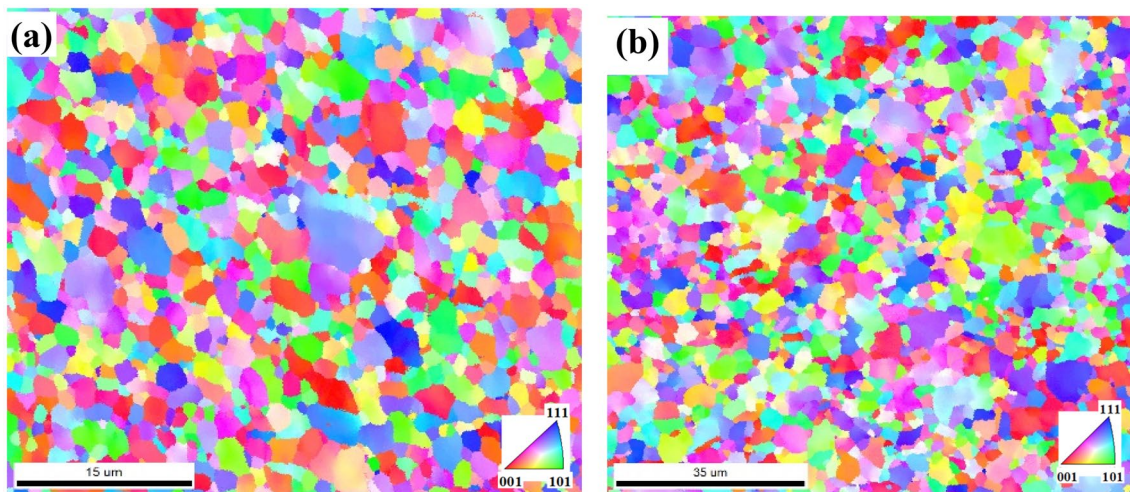
Fig. 3 Microstructures (inverse pole figure (IPF) map from EBSD) of 304L SS friction-stirred top surface: **a** friction stir welded at 725 °C (mean grain size 2.4 ± 0.9 µm) and **b** friction stir welded at 825 °C (mean grain size 4.2 ± 1.6 µm)

with the grain growth that was more pronounced at 825 °C than at 725 °C. Grain size distribution analysis of 825 °C SZ revealed that the area fraction of submicron size grains was less than 5% throughout the SZ. The amount of LAGB in 825 °C SZ was less than that obtained in the 725 °C SZ because of higher tool rotation [32]. At a lower rpm condition, due to frictional heat, the dislocations could easily group to form low-angle boundaries (referred to as polygonization) in larger numbers than that occurred in a higher rpm condition because of the low energy condition. The low-angle boundaries are sub-grain structures and consist of linear dislocation arrays. A low-angle boundary moves as a unit under shear stress [33].
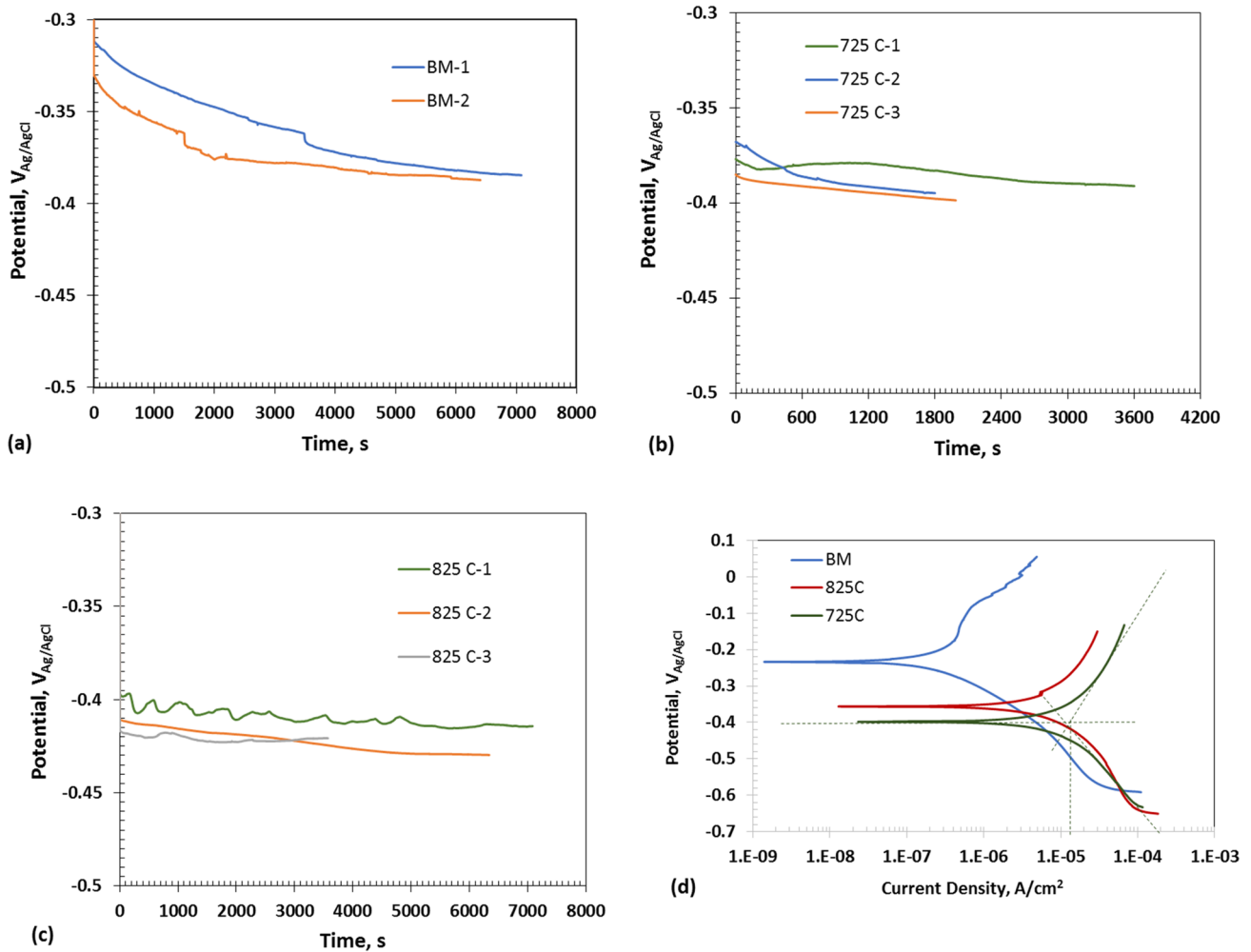
Fig. 4 Open-circuit potential as a function of time of stainless steel specimens in 3.5% NaCl solution at room temperature: **a** 304L base metal, **b** friction-stirred zone at isothermal tool temperatures at 725 °C and **c** 825 °C samples. **d** The polarization plots for evaluating Tafel slopes

Table 3 The comparison of OCP and linear polarization resistance values for the base metal, SZ at 825° C, and SZ at 725° C friction stir crack-repaired samples

Sample	OCP (V)	R_p (kilo ohms)	Anodic Tafel slope (β_a) (V/decade)	Cathodic Tafel slope (β_c) (V/decade)	Corrosion current density (i_{corr}) (µA/cm^2)
Base metal	−0.38±0.015	15.62–16.28	0.16–0.2	0.12–0.16	1.9–2.4
SZ-725 °C	−0.39±0.010	6.15–7.53	0.22–0.26	0.42–0.47	8.1–12.2
SZ-825 °C	−0.41±0.025	3.87–4.23	0.41–0.44	0.38–0.4	12–19

3.2 Corrosion under open-circuit condition

The plots of open-circuit potential as a function of time are shown in Fig. 4a and c. The steady-state open-circuit potentials of the specimens in 3.5% NaCl solution are summarized in Table 3. Open-circuit potential (OCP) or the corrosion potential is a mixed potential at which the rate of anodic reactions equals the rate of cathodic reaction. Since there was no deaeration of the electrolyte, the predominant cathodic reaction could be reduction of dissolved oxygen in the solution, and the anodic reaction was oxidation of the stainless steel. Formation of a passive film on the specimen will increase the polarizability and increase the anodic Tafel slope which, in turn, will shift the OCP in the more positive direction if the cathodic reaction rates do not change. Therefore, the values of OCP will be an indication of the reactivity or passivity of the specimens in a given environment. The more positive the OCP, the more passive will be a material. The OCP shifted in the negative direction with the increase in time and reached a plateau value for all the specimens. The OCP of SZ-825 °C stirred sample is the most negative followed by SZ-725 °C. Therefore, it can be stated that the SZ-825 sample is the most corrosion prone in open-circuit condition, whereas the base metal is the least corrosion prone in the 3.5% NaCl solution. Also, the OCP of SZ-825 sample showed significant fluctuation before reaching a quasi-steady-state conditions as shown in Fig. 4c. The OCP or corrosion of the 304L SS base metal was found to be around − 380 mV. This value is consistent with previously reported OCP value in the same aqueous sodium chloride medium. A similar value of − 372 mV for the OCP was reported by Heakal et al. [34]. The linear polarization resistance is another indicator to describe the corrosion resistance of a metal. The higher the polarization resistance, R_p, the higher the resistance toward corrosion. The R_p values for the different specimens are listed in Table 3, which follows the same trend observed for the OCP values. The 304L SS base metal showed the highest resistance toward the polarization or better corrosion resistant than that of SZ-725 and SZ-825 specimens. Figure 4c shows the Tafel plots of the 304L base metal and FSW samples in 3.5% NaCl solution. The Tafel slopes of cathodic (β_c) and anodic (β_a) branches were evaluated by considering the linear portion of the log i vs. potential plots. The corrosion current density i_{corr} is related to cathodic and anodic Tafel's slope (β_c, β_a) and R_p (ohm.cm^2) values and can be expressed as [35]:

$$i_{corr} = (\beta_c * \beta_a) / (2.303 (\beta_c + \beta_a) R_p). \tag{1}$$

The values of β_c, β_a, R_p, and i_{corr} are summarized in Table 3. The FSW specimens showed steeper anodic and cathodic Tafel slopes than the base metal indicating an increased
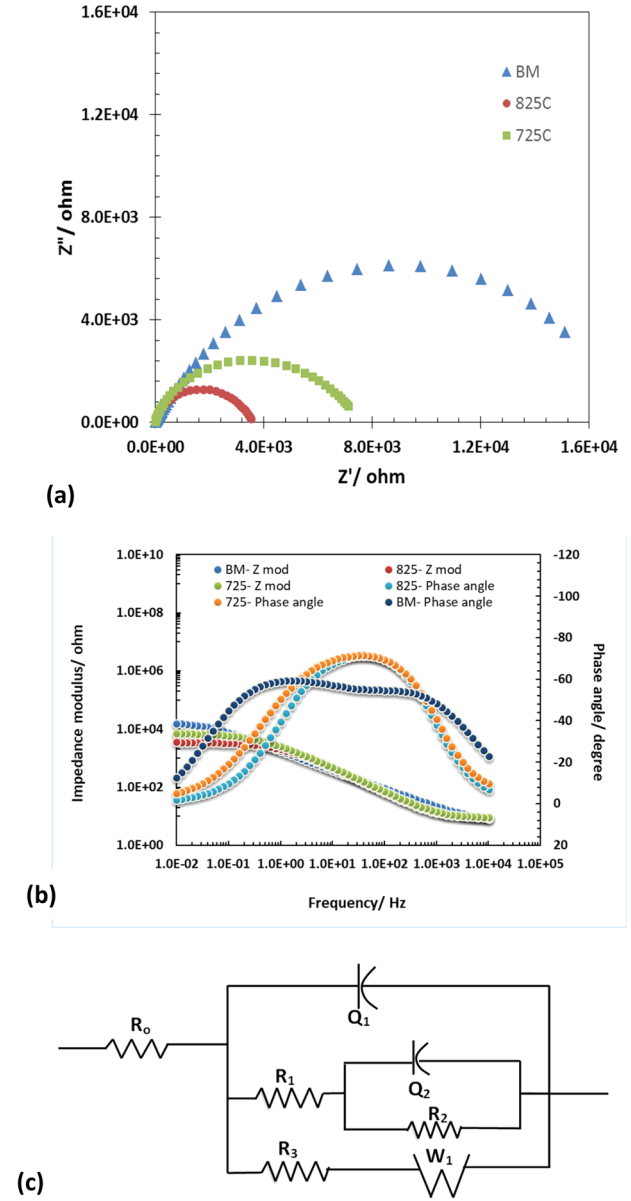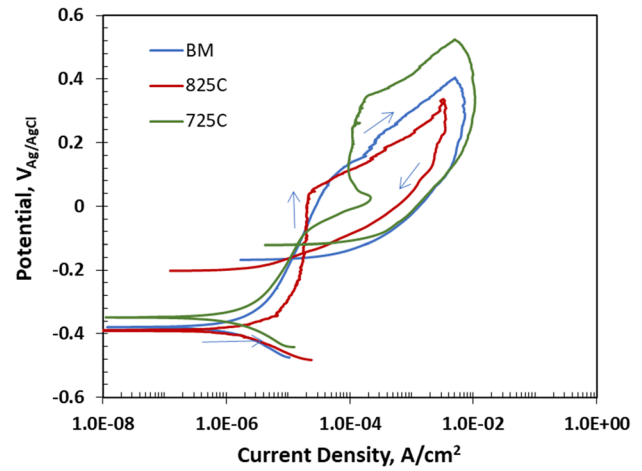

(a)

(b)

(c)

Fig. 5 Results of electrochemical corrosion tests of 304L base metal, and friction-stirred zone at isothermal tool temperatures at 825 °C and 725 °C samples (referred to as 850 °C and 725 °C, respectively) in 3.5% NaCl solution at room temperature. Electrochemical impedance spectra **a** Nyquist plots at OCP, **b** Bode plots at OCP, and **c** electrical equivalent circuit

polarizability after plastic deformation, possibly due to the presence of more active sites for film formation on the specimens. The SZ-825 specimen showed the highest corrosion rate among the specimens investigated because the i_{corr} value was influenced by the lower R_p and steeper Tafel slopes.

Figure 5a shows the EIS data as Nyquist plots and Bode plots which are shown in Fig. 5b. The (depressed) semicircles observed in the Nyquist plots reflect the

electrochemical interfacial behavior influenced by the material properties including microstructural inhomogeneity, presence of inclusions, etc. [36], which is fundamentally related to the corrosion behavior of the material. The EIS data were fitted with several electrical equivalent circuits (EECs) using the commercially available software program called *Echem Analyst* available through Gamry Instruments, Inc., USA, and a suitable model was chosen based on the goodness of fitting value. The EIS data were fitted with an EEC having two time constants. Even though the Nyquist plots appear to have only one time constant, the Bode plots exhibited two time constants as seen from the phase angle plots, specifically that of the base metal. After examining several types of EECs with one and two time constants, the EEC illustrated in Fig. 5c was considered to represent the EIS data better. The corresponding values of the equivalent electrical circuit (EEC) elements are listed in Table 4. The fitted values of the charge transfer resistance, R_1, obtained from Table 4, are in a good agreement with the R_p value listed in Table 3. In the equivalent circuit, R_0 represents the electrolyte resistance, R_1 represents the charge transfer resistance or polarization resistance, and Q_1 represents interfacial leaky capacitance whose impedance (Z) is given by the relation: $Z = 1/[(j\omega)^a Q_1]$ where $j = \sqrt{-1}$, ω = frequency, and the exponent 'a' represents the surface heterogeneity or continuously distributed time constants for charge transfer when $a < 1$. The second 'RC'-type loop consisting of R_2 and Q_2 components represents the defect structure of the passive film. The Q_2 could be related to the lumped capacitance developed due to high grain boundary area of the thin passive film. An epitaxial-type growth of passive film is assumed here,


Fig. 6 Results of cyclic polarization tests of 304L base metal, and friction-stirred zone at isothermal tool temperatures at 825 °C and 725 °C samples (referred to as 850 °C and 725 °C, respectively) in 3.5% NaCl solution at room temperature

and therefore the grain size of the passive film is correlated with the grain size of the substrate. It is noted that the Q_2 values of FSW specimens were three orders of magnitude higher than that of base metal specimen. The EIS behavior of the base metal did not include the circuit elements R_3 (a resistor) and W_1 (Warburg element) representing diffusion-controlled impedance behavior. These elements were part of the EIS behavior of FSW specimens which could be associated with the high fraction of low-angle grain boundaries in the substrate. The alignment of dislocations that formed low-angle grain boundaries in the substrate could be a source of misorientation dislocations at the metal/

Table 4 The values of electrical equivalent circuit (EEC) elements fitted with the EIS data of the specimens after 1-h immersion in 3.5% NaCl solution at OCP

Specimen ID	R_0 (ohm)	$Q_1/10^{-6}$ (S.s^a)	a	R_1 (ohm)	$Q_2/10^{-3}$ (S.s^b)	b	R_2 (ohm)	R_3 (ohm)	$W_1/10^{-6}$ (S.s$^{0.5}$)	$\chi^2/10^{-6}$
Base metal	6.3	90	0.72	16,480	0.055	0.75	422	–	–	0.6
SZ-725 °C	9.4	48.5	0.87	7512	26.6	1.0	785	43.4	40.7	51
SZ-825 °C	9.3	51.6	0.88	3651	58.2	1.0	1117	5.2	36.3	36
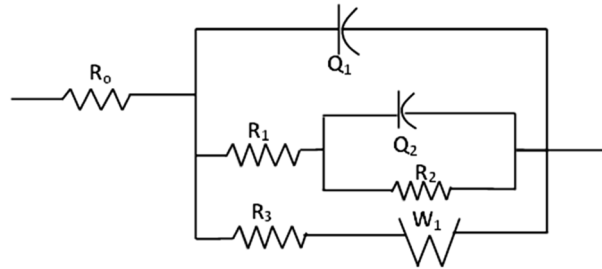
film interface [37]. Burgers vector of these dislocations will be normal to the interface plane (that is the reason it is called misorientation) and create monoatomic ledges at the interface. Anion vacancies could be created when climb occurs in these dislocations. Therefore, the climb of misorientation dislocations results in localized growth of oxide [37]. This entire process including the dislocation climb is assumed to be diffusion-controlled and represented by the Warburg element. The oxide growth process occurring by lateral climb of misorientation climb is considered not to induce stress in the metal substrate [37]. The EIS spectra followed a similar trend that is observed in the linear polarization studies. These findings clearly give a better idea that the base metal is more resistant to corrosion compared to the crack-repaired samples by friction welding.
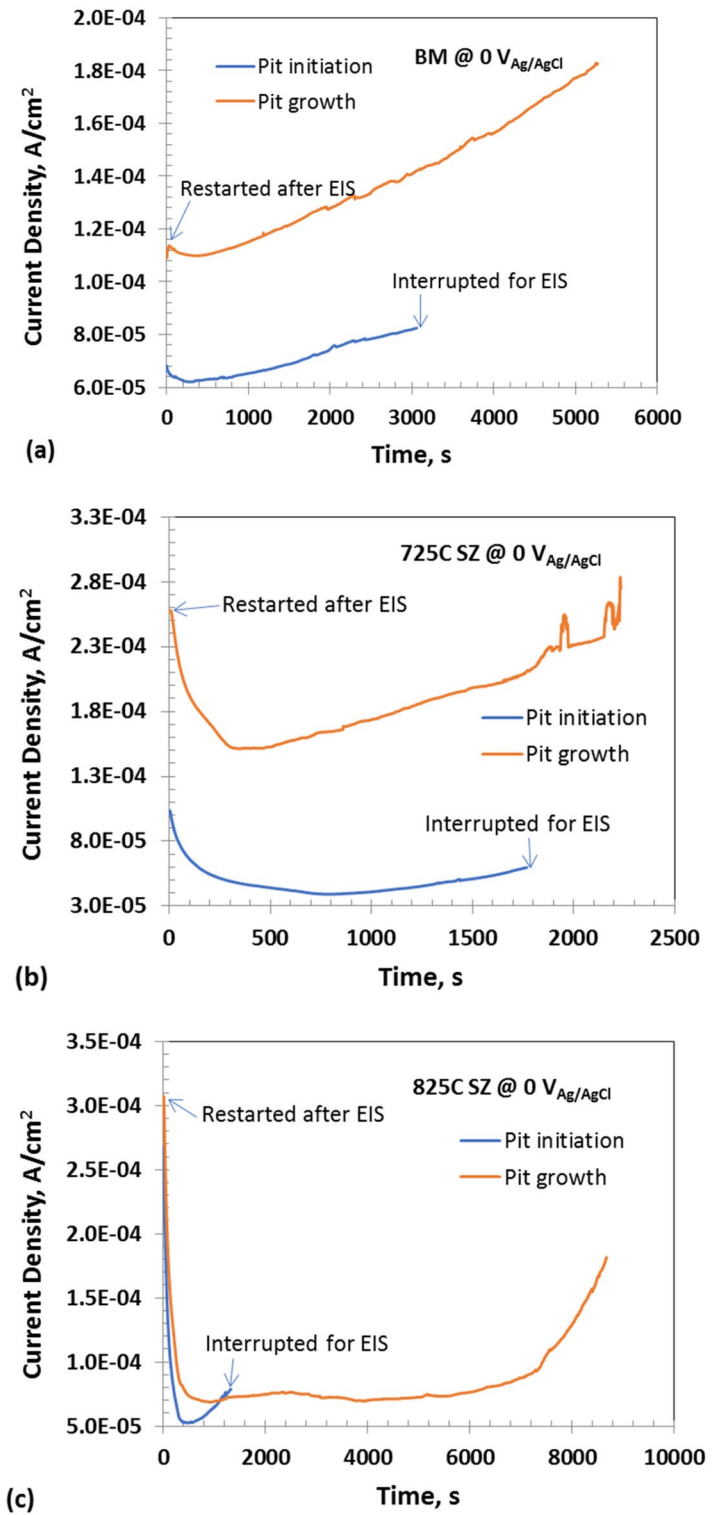
3.3 Cyclic polarization

Figure 6 shows the cyclic polarization plots for the three different specimens. The cyclic polarization plot gives us an idea about the pitting behavior of the material. It is well established that 304L-type austenitic steels are prone to the pitting corrosion in the presence of sea water (3.5% NaCl) [2, 35, 38]. The cyclic polarization test carries the information about the pitting protection potential (E_{pp}), the breakdown or transpassive potential (E_b), and passive current density (i_{pass}). During the forward potential scan in the anodic direction, the current density does not increase significantly or remains almost a constant in the case of the SZ-825 sample, until a threshold potential is reached, as shown in Fig. 6. A protective surface film forms during polarization at this potential window. Thickening of passive film is anticipated as the potential increases which could be associated with accumulation of point defects and incorporation of chloride ions in the passive layer. After reaching a threshold potential, the current density increased sharply indicating a shoulder or knee in the polarization plot. This shoulder potential is denoted as passivity breakdown potential (E_b) beyond which the passive film is unstable and is not protective. Pits are considered to initiate and grow when polarization continued above this potential. After reaching a predetermined

current density (5 mA/cm^2 in this study), the direction of the polarization is reversed. If the pits were quickly passivated, the reverse log I-V plot would trace the forward log I-V plot without showing any hysteresis. On the other hand, if active dissolution was occurring within the pits, then the current density during the reverse scan would be higher than that of forward scan for a given potential. This would show a hysteresis behavior as shown in Fig. 6. After reaching a critical potential during the reverse scan, the pits repassivate completely and exhibit a lower current density than that of the forward scan. At this potential, the reverse log I–V plot crosses over the forward plot. The crossover potential is denoted as pitting protection potential (E_{PP}). It is noted that the E_{PP} shows negative potentials and is closer to the corrosion potential. The EPP value will change as a function of apex current density (at which the polarization direction is reversed), scan rate, and pH of the solution. Increase in apex current density, and decrease in pH of the solution will result in more negative E_{PP} values. More positive E_{PP} values could be observed for shallow pits since these can be repassivated faster than pits with high aspect ratio. The E_{PP} is the potential below which no new pits can initiate. At potentials more positive than the E_b or breakdown potential, the pits can form and grow exponentially causing a severe degradation of the material [39]. Passive current density (i_{pass}) provides the information about the passivity of the specimens; the lower the current density, the better is the passivity and higher the corrosion resistance. The exchange current densities of oxygen reduction reaction and iron dissolution were calculated from the cathodic and polarization plots, respectively. The $i_{0,ORR}$ was estimated by extrapolating the linear portion of the cathodic polarization to the redox potential of the oxygen reduction reaction ($E^0_{ORR} = 0.7055$ V$_{Ag/AgCl}$). Here, oxygen reduction was the only reaction considered to occur as the cathodic reaction on the specimen surface. The anodic reaction is the dissolution of the stainless steel. However, for the exchange current density estimation, it is assumed that iron is the predominantly dissolving element, and therefore the linear portion of the anodic plot was extrapolated to the redox potential of Fe $\rightarrow$ Fe^{2+} + 2e$^-$; $E^0 = -0.64$ V$_{Ag/AgCl}$. The exchange current densities give an idea about the general corrosion behaviors of the

Table 5 Summary of the cyclic polarization results of the base metal, SZ at 825 °C, and SZ at 725 °C

Sample	Pitting protection potential E_{pp}(mV$_{Ag/AgCl}$)	Transpassive potential E_b(mV$_{Ag/AgCl}$)	Passivation current density i_{pass} (µA/cm^2)	Exchange current density for oxygen reduction reaction ($i_{0,ORR}$, A/cm^2)	Exchange current density for iron dissolution ($i_{0,Fe}$, A/cm^2)
Base metal	− 152 ± 12	116 ± 15	3.8–65	1.5–4 × 10^{-10}	2–4.2 × 10^{-9}
SZ-725^{0}C	− 114 ± 8	− 78 ± 6	3.4–19.5	1–2 × 10^{-10}	4–6 × 10^{-6}
SZ-825^{0}C	− 146 ± 12	46 ± 8	− 20	1.5–3 × 10^{-8}	2–4 × 10^{-6}

Fig. 7 Results of potentiostatic tests at 0 $V_{Ag/AgCl}$ in 3.5% NaCl solution at room temperature. **a** Base metal, **b** stirred zone (SZ) under 725 °C isothermal condition, and **c** SZ at 825 °C

materials. Higher exchange current density indicates higher activity for corrosion.

Table 5 summarizes the values of E_{pp}, E_b, i_{pass}, and i_0 for three different samples derived from the cyclic polarization data. This comparison revealed that among the three specimens investigated, the base metal shows the lowest E_{pp} and the SZ-725 °C sample the highest E_{pp}. The E_{pp} value of base metal (− 152 mV) was similar to the previously reported values [40]. The E_{pp} values observed on all three specimens were about 200 mV more positive than that of their corrosion potentials in the 3.5% NaCl solution. This observation indicated that the presence of oxidizers

Table 6 The pit initiation time and pit growth time at 0 $V_{Ag/AgCl}$ for the base metal, 825 °C and 725 °C friction stir crack-repaired samples

| Sample	Pit initiation time (s) (to reach 80 μA/cm²)	Pit growth time (s) (to reach 180 μA/cm²)
Base metal	2712±330	5158±270
SZ-725 °C	2320±80	1132±354
SZ-825 °C	1540±64	8654±660

in the 3.5% NaCl environment that increases the corrosion potential of the 304L would lead to pitting. FSW did not increase the pitting resistance. On the other hand, FSW decreased the breakdown potential (E_b) due to the presence of lazy-S, as shown in Table 5. Both the base metal and SZ-725 specimens showed the same order of passivation current density, while the SZ-825 specimen showed a marginally higher passivation current density than other two cases. The SZ-725 specimen showed an increase in the

current density at potentials anodic to − 80 mV$_{Ag/AgCl}$ (primary transpassive potential) that reached a peak value of 211 μA/cm² at 30 mV$_{Ag/AgCl}$. The increase in current density could be due to localized attack on the lazy-S feature of the ZS-725 specimen. The SZ-825 specimen also consisted of a lazy-S feature with a higher surface area than that of the lazy-S of the SZ-725. Therefore, attack on the more localized lazy-S of the SZ-825 specimen which started at potentials more anodic to 40 mV continued monotonically, revealing a transpassive behavior. On the other hand, the SZ-725 specimen repassivated after showing a peak current because of a relatively smaller area and less localized nature of the lazy-S present in the SZ-725 specimen. However, the second passivation showed much higher current density (~ 110 μA/cm²). Because of the secondary passivation, the transpassive potential or passivity breakdown potential of the SZ-725 specimen could be considered as 350 mV$_{Ag/AgCl}$. However, the primary transpassive potential of the SZ-725 was around − 80 mVAg/AgCl as listed in Table 5. It should be noted that the theoretical oxygen
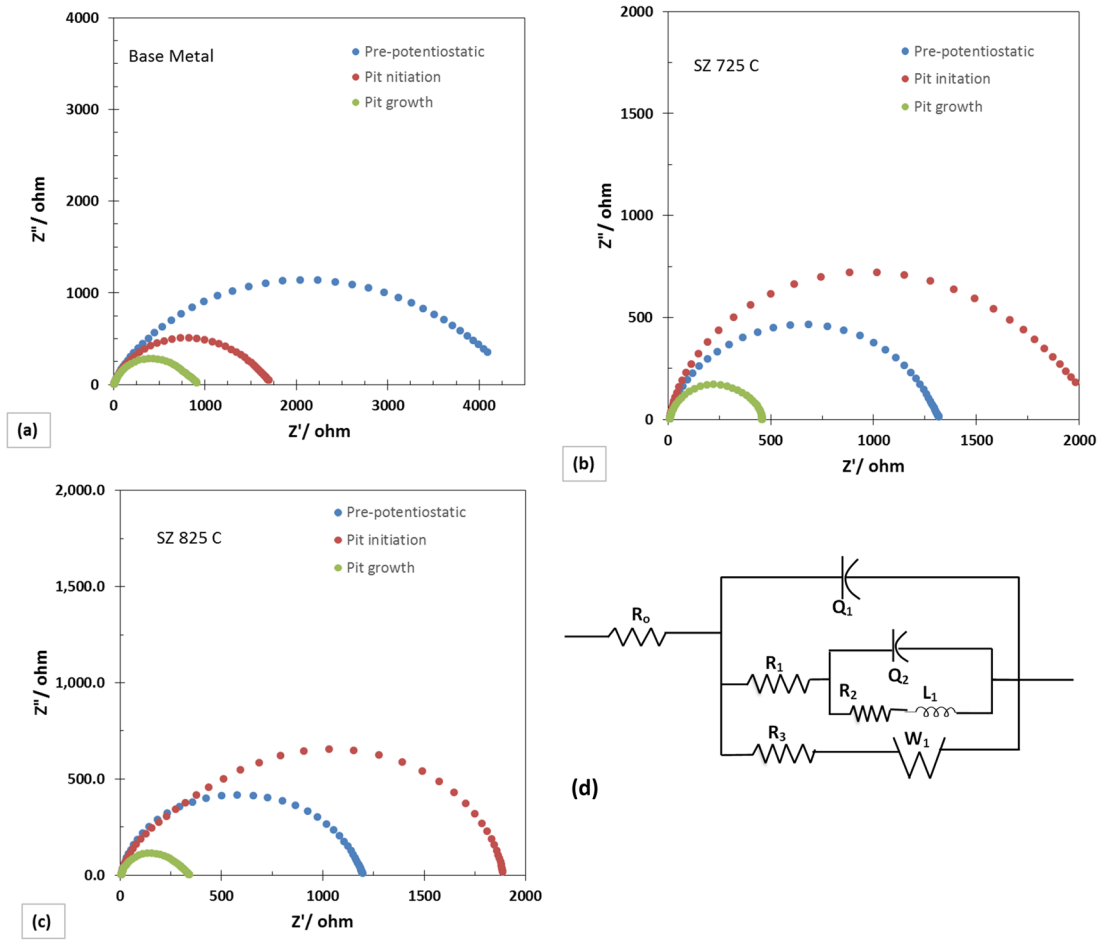
Fig. 8 Results of Nyquist plots (potentiostatic EIS data) at 0 V$_{Ag/AgCl}$ in 3.5% NaCl solution at room temperature in three different time intervals such as at $t=0$ (pre-potentiostatic), after pit initiation, and pit growth: **a** base metal, **b** stirred zone (SZ) under 725 °C isothermal condition, **c** SZ at 825 °C, and **d** equivalent electric circuit (EEC) fitting the EIS data
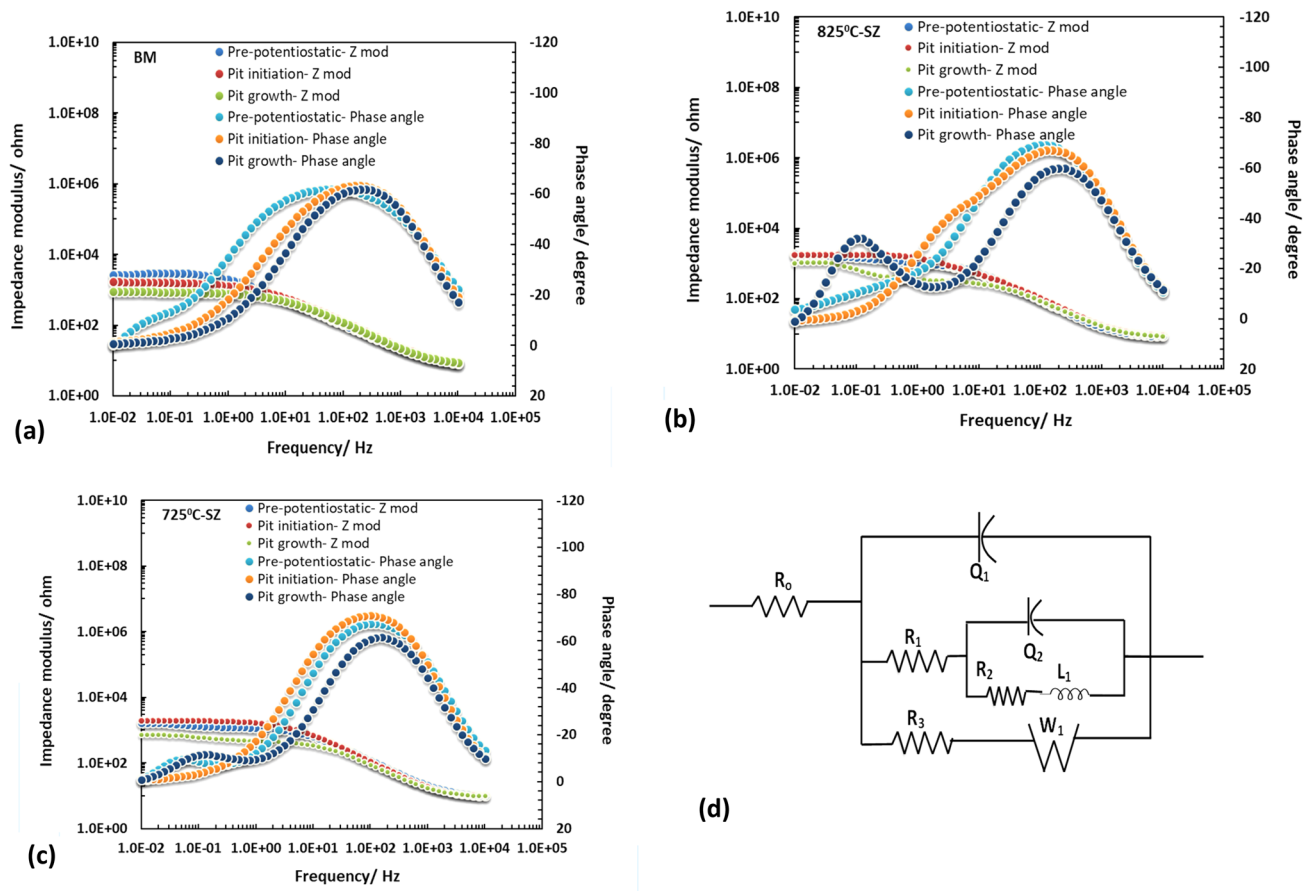
Fig. 9 Results of Bode plots (potentiostatic EIS tests) at 0 $V_{Ag/AgCl}$ in 3.5% NaCl solution at room temperature in three different time intervals such as at $t=0$ (pre-potentiostatic), after pit initiation, and pit growth: **a** base metal, **b** stirred zone (SZ) under 725 °C isothermal condition, **c** SZ at 825 °C, and **d** equivalent electric circuit (EEC) fitting the EIS data

Table 7 The values of electrical equivalent circuit (EEC) elements fitted with the EIS data of the base metal (BM) specimens after potentiostatic tests at 0 $V_{Ag/AgCl}$ in 3.5% NaCl solution
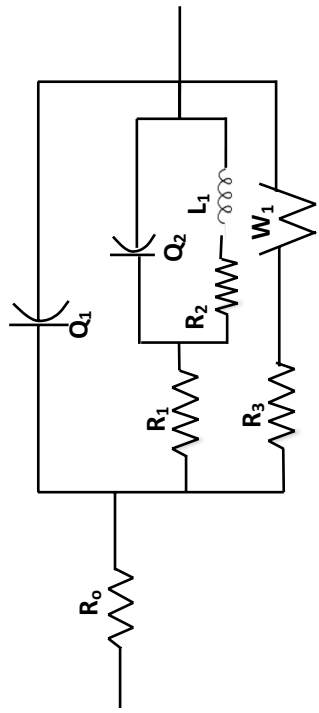

Specimen ID	R_0 (ohm)	$Q_1/10^{-6}$ (S.s^a)	a	R_1 (ohm)	$Q_2/10^{-6}$ (S.s^b)	b	R_2 (ohm)	$\chi^2/10^{-6}$
BM—start	7.6	98.2	0.49	4482	42.3	0.81	545	0.6
BM—pit initiation	9.3	23.2	0.85	1666	68.6	0.545	30.2	296
BM—pit growth	7.7	41.5	0.815	587.6	584	0.43	324.5	126

evolution potential in the 3.5% NaCl (pH 5.5) is around 700 mV$_{Ag/AgCl}$. Therefore, the increase in the current density at high anodic potentials corresponds to the passivity breakdown and not because of the oxygen evolution reaction. The cyclic polarization results showed only marginal difference in the pitting protection potentials and the transpassive potentials of the specimens. The resistance to pitting corrosion of the specimens followed more

Table 8 The values of electrical equivalent circuit (EEC) elements fitted with the EIS data of the SZ-725 °C specimens after potentiostatic tests at $0\,V_{Ag/AgCl}$ in 3.5% NaCl solution

Specimen ID	R_0 (ohm)	$Q_1/10^{-6}$ (S.s^a)	a	R_1 (ohm)	$Q_2/10^{-3}$ (S.s^b)	b	L_1 (henry)	R_2 (ohm)	R_3 (ohm)	$W_1/10^{-6}$ (S.s$^{0.5}$)	$\chi^2/10^{-3}$
SZ-725 °C—start	9.7	22.4	0.89	1376	10	1.0	–	364.5	268.3	45.6	5.9
SZ-725 °C—pit initiation	9.4	25	0.9	1967	90	1.0	0.122	5880	0.2	28.8	1.4
SZ-725 °C—pit growth	9.3	28	0.9	492	9.8	0.68	7.97	235	1.7	70	6.6

or less a similar trend that was observed for general corrosion at the open-circuit condition. The results of polarization resistance and cyclic polarization did not give an unequivocal point of view on how the plastic deformation by FSW process affected the corrosion resistance of the material. On the other hand, the exchange current densities for oxygen reduction reaction (ORR) and iron oxidation exhibited some dependency of plastic deformation. For example, the $i_{0,ORR}$ and $i_{0,Fe}$ of SZ-825 C were two and three orders of magnitude larger than those of base metal, respectively. The ORR activity of SZ-725 was similar to that of base metal, while the $i_{0,Fe}$ was similar to that of SZ-825 C. Therefore, it can be concluded that heavy plastic deformation increased the activity for iron oxidation by three orders of magnitude when compared to that of annealed base metal.

In order to better understand the effect of microstructural changes occurred in the FSW process, the results of potentiostatic tests are presented in the next section.

3.4 Potentiostatic passivation

Potentiostatic tests are carried out at a constant potential of 0 V vs Ag/AgCl on each sample in order to understand the behavior of the passive film forming on the surface when immersed in the 3.5% NaCl solution. The 0 V vs Ag/AgCl was selected for the potentiostatic conditioning because this potential was more positive than the pitting protection potentials (E_{pp}) of all the samples, and therefore pitting can be easily initiated. The time taken for pit initiation may be used for ranking the materials prepared under different conditions. In the potentiostatic tests, the current was recorded as a function of time. Formation of an impervious passive film resulted in a current decay behavior. The presence of any current spikes indicated events of localized rupture of the passive film. Instead of decaying, if the current started to rise, then pit initiation and growth were considered. Figure 7a–c shows the I-t plot recorded during the potentiostatic test. An initial decay of current was observed for the first few hundred seconds in all the specimens. The absence of abrupt current spikes during the initial decay period indicated that the passive film was stable. After the initial passivation, the current slowly started increasing. If the current density was higher than 20 μA/cm², pit initiation was considered to have occurred. This value of current density was chosen to signify pit initiation because the cyclic polarization tests showed that the passivation current density was typically around 10 μA/cm². When the current density reached about 80 μA/cm², the test was interrupted and EIS and Mott–Schottky analyses were carried out to evaluate the electrochemical properties of the passive film after pit initiation. After these tests, the potentiostatic conditioning continued until reaching

a current density of 180 μA/cm² or more, which considered as pitting growth stage. The pit initiation (to reach 80 μA/cm²) and growth (to reach 180 μA/cm²) times were recorded for each sample and presented in Table 6. The base metal specimens showed longer pit initiation time than other two specimens. Pit growth occurred faster in the SZ-725 C specimen than in other two cases, whereas the SZ-825C showed the longest time required to reach a current density of 180 μA/cm² at 0 V Ag/AgCl at room temperature.

EIS and Mott–Schottky analysis were performed in pre-potentiostatic (after stabilizing at the OCP and conditioning at 0 $V_{Ag/AgCl}$), pit initiation (after reaching 80 μA/cm²), and pit growth conditions in order to determine the defect structure of the passive film. The EIS spectra (Nyquist plots) of the specimens are shown in Fig. 8a–c. The corresponding Bode plots are shown in Fig. 9a–c. A general fitted electrical equivalent circuit is shown in Fig. 8d, but not all elements were present in each test condition. The impedance of the base metal specimen decreased at every step of evaluation as shown in Fig. 8a and Fig. 9a. The frequency at which the peak in the phase angle occurred shifted to higher values as the pit initiation and growth were observed as shown in Fig. 9a. The range of frequencies for capacitor-like behavior decreased with the pit initiation and pit growth. Table 7 summarizes the values of the EEC components. The EIS spectra of the base metal specimens could be fitted with a single EEC of a porous film type with two RQ loops. The Q_1 value representing the interfacial capacitance decreased during pit initiation and growth as compared to that of the starting condition. On the other hand, Q_2, which is associated with the defect structure, increased with the increase in time under potentiostatic conditioning. At very low frequencies, the effective resistance could be given as summation of all the resistor values. The effective resistance decreased with an increase in the exposure time which indicated degradation of the passive film or passivity breakdown. Figures 8b and 9b show EIS spectra of the SZ-725 °C specimens conditioned at 0 $V_{Ag/AgCl}$ at three different time intervals. The impedance increased when the current density reached a value of 80 μA/cm² in contrast to that observed with the BM specimens. The increase in the impedance indicated that the passive film of the SZ-725 °C specimen was not impaired in spite of the increase in the current density. The observed current density was attributed to the dissolution of the lazy-S region. Microstructure of the specimen observed after the test supported this claim which will be discussed in a later section. The EIS data were fitted with an EEC, and the values of the EEC elements are summarized in Table 8. The EEC of the potentiostatic condition is different from that of the OCP condition because it includes an inductor (L_1) element in the RQ loop. The inductor represents the

Table 9 The values of electrical equivalent circuit (EEC) elements fitted with the EIS data of the SZ-825 °C specimens after potentiostatic tests at 0 $V_{Ag/AgCl}$ in 3.5% NaCl solution
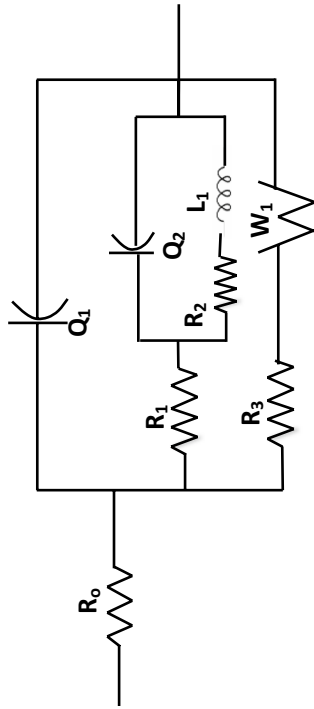
Specimen ID	R_0 (ohm)	$Q_1/10^{-6}$ (S.s^a)	a	R_1 (ohm)	$Q_2/10^{-6}$ (S.s^b)	b	L_1 (henry)	R_2 (ohm)	R_3 (ohm)	$W_1/10^{-6}$ (S.s$^{0.5}$)	$\chi^2/10^{-3}$
SZ-825 °C—start	18.6	2.6	0.6	8.5	33.8	0.88	–	1972	1639	268	5.3
SZ-825 °C—pit initiation	8.35	29.7	0.89	467.5	52.5	1.0	8.3×10^{-6}	1948.5	321	27.8	3.4
SZ-825 °C—pit growth	9.3	20.3	0.94	368.7	290	1.0	2.16	733.7	20.17	120	5.2
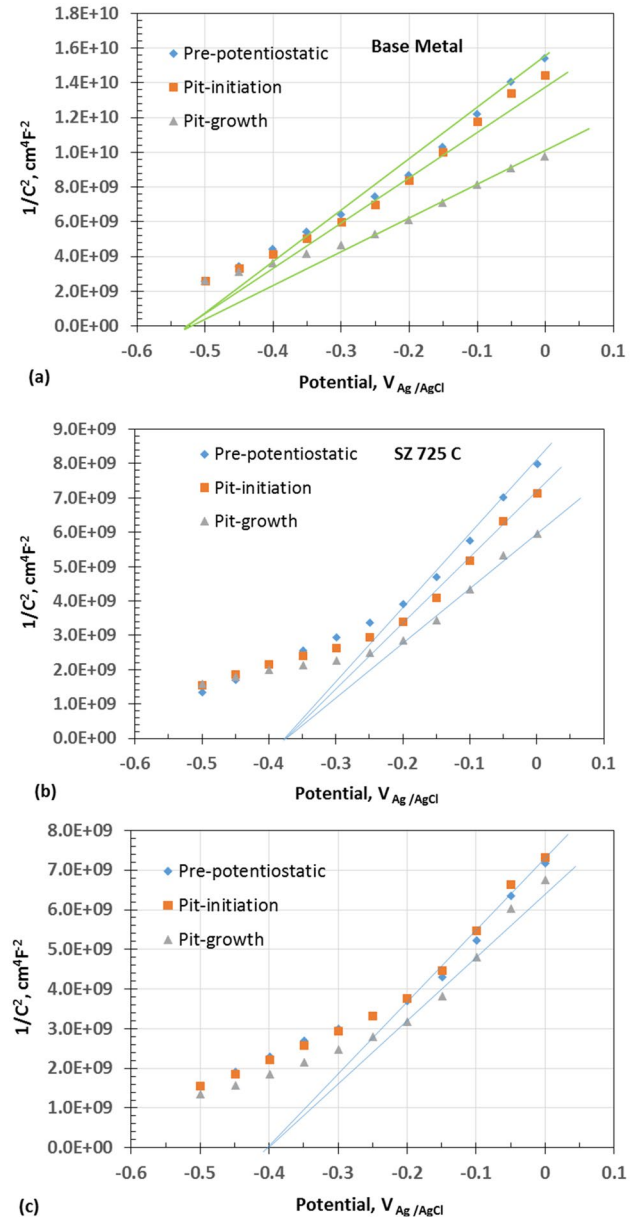
Fig. 10 Mott–Schottky plots of specimens conditioned at 0 $V_{Ag/AgCl}$ in 3.5% NaCl solution at room temperature. **a** Base metal, **b** stirred zone (SZ) under 725 °C isothermal condition, and **c** SZ at 825 °C

adsorption of chloride ions in the defect structures. Point defects such as anion vacancies (V_O^{2+}) could be preferential sites for chloride ion adsorption following the reaction [41]:

$$V_O^{2+} + Cl^- \rightarrow Cl_O^+. \tag{2}$$

The presence of an inductor in the EIS of FSW specimens but not in the BM specimens indicated that the lazy-S defect played a crucial role in the adsorption

phenomenon. The adsorption has a unit of ohm.s, and therefore, at low frequencies the impedance due to an inductor is very low. At low frequencies, the impedance is determined mainly by the resistor elements. The impedance values of the SZ-725 °C increased during 'pit-initiation' and decreased significantly during the pit growth condition.

Figures 8c and 9c show EIS spectra of the SZ-825 °C specimens under potentiostatic conditioning at $0\,V_{Ag/AgCl}$. The impedance behavior followed a similar trend of that observed with the SZ-725 °C specimens, where the impedance increased during the 'pit-initiation' period probably because the dissolution of the lazy-S zone did not result in passivity breakdown. When the current density was ~ 200 µA/cm^2, the impedance decreased significantly. Table 9 lists the values of the components of EEC fitted with the EIS data. The impedance of the SZ-825 °C specimen was lower than that of SZ-725 °C under each test condition.

Figure 10a–c shows the Mott–Schottky (M-S) plots of the BM, SZ-725 C, and SZ-825 C specimens carried out at different time intervals during the potentiostatic conditioning at $0\,V_{Ag/AgCl}$. Passive films of the specimens showed an *n*-type semiconductivity because of the positive slopes observed in the M-S plots. The intercept of the linear region at $1/C^2 = 0$ could be considered as the flat band potential. It is noted that the flat band potential did not change with the increase in the exposure time in all the specimens. The flat band potential gives an idea about the Fermi energy level of the passive film, and the potential at which no band bending occurs and no space charge layer is present. The information on flat band potential, along with the band gap energy of the passive film, and charge carrier density, can be used to estimate the stability of the passive film under anodic or cathodic polarization conditions [42]. The energy level of the conduction band minimum (CBM) of the passive film can be calculated based on the flat band potential [43]. The energy level of the CBM determines the energetics of water reduction reaction which is one of the cathodic reactions of stainless steel corrosion. Negative shift of the flat band potential will enhance the water or hydrogen reduction reactions. Charge carrier density of the passive film is

calculated from the slope of the linear portion (closer to the film formation potential) and listed in Table 10. The FSW specimens showed less negative flat band potential than that of base metal. The charge carrier density of the passive film formed on the BM specimen was less than that of FSW specimens under identical test conditions and was in the range of $3.7–6.1 \times 10^{20}$ cm^{-3}. The charge carrier density increased with an increase in the exposure time for all the specimens indicating aging effect of the passive film. The charge carrier density of the SZ-725 C increased from 5.6×10^{20} cm^{-3} to 6.0×10^{20} cm^{-3} after about 30 min of conditioning at $0\,V_{Ag/AgCl}$ and to 7.2×10^{20} cm^{-3} after about 4200 s of total exposure time. The SZ-825 °C specimen also showed a marginally higher carrier density than that of the SZ-725 °C specimen in each test condition.

Figure 11a–c shows the optical microstructures of the specimens after potentiostatic conditioning. The specimens were slightly etched to reveal the grain boundaries so that the pit initiation sites could be revealed. It is seen from Fig. 11a that the pits were initiated inside the grains in the case of the base metal. Figure 11b and c reveals preferential attack on the lazy-S zones of the SZ-725 °C and SZ-825 °C specimens, respectively. Figure 12a–d shows the SEM images of the microstructures of the specimens under similar test conditions as that of Fig. 11. Delta ferrite stringes are observed in the BM specimens as shown in Fig. 12b. It is noted that pits initiated inside the grains randomly as shown in Fig. 12a. Pit initiation was not observed either inside the delta ferrite stringes or at the interface between the ferrite/austenite. Therefore, compositional gradient of chromium or other ferrite-stabilizing elements did not deleteriously affect the pitting resistance of this material. Pit-like features could be observed on the lazy-S zone of the SZ-825 °C specimen as illustrated in Fig. 12c and d. Figure 13a and b shows the optical micrographs of the SZ-825 °C specimen before and after potentiostatic conditioning. The pit size and distribution could be seen at a current density of 200 µA/cm^2 in the SZ-825 °C.

Table 10 Charge carrier densities and flat band potentials of the passive film formed under potentiostatic conditioning at $0\,V_{Ag/AgCl}$ at different time intervals

| Specimen	Charge carrier density, cm^{-3}			Flat band potential, $V_{Ag/AgCl}$
	Testing condition			
	Pre-potentiostatic, at $t = 0$ s	After pit initiation	After pit growth	
Base metal	$3.7 \pm 0.8 \times 10^{20}$	$4.2 \pm 0.4 \times 10^{20}$	$6.1 \pm 0.3 \times 10^{20}$	-0.525 ± 0.03
SZ-725 °C	$5.6 \pm 0.4 \times 10^{20}$	$6.0 \pm 0.2 \times 10^{20}$	$7.2 \pm 0.2 \times 10^{20}$	-0.375 ± 0.02
SZ-825 °C	$6.6 \pm 0.6 \times 10^{20}$	$6.9 \pm 0.3 \times 10^{20}$	$7.3 \pm 0.4 \times 10^{20}$	-0.4 ± 0.016
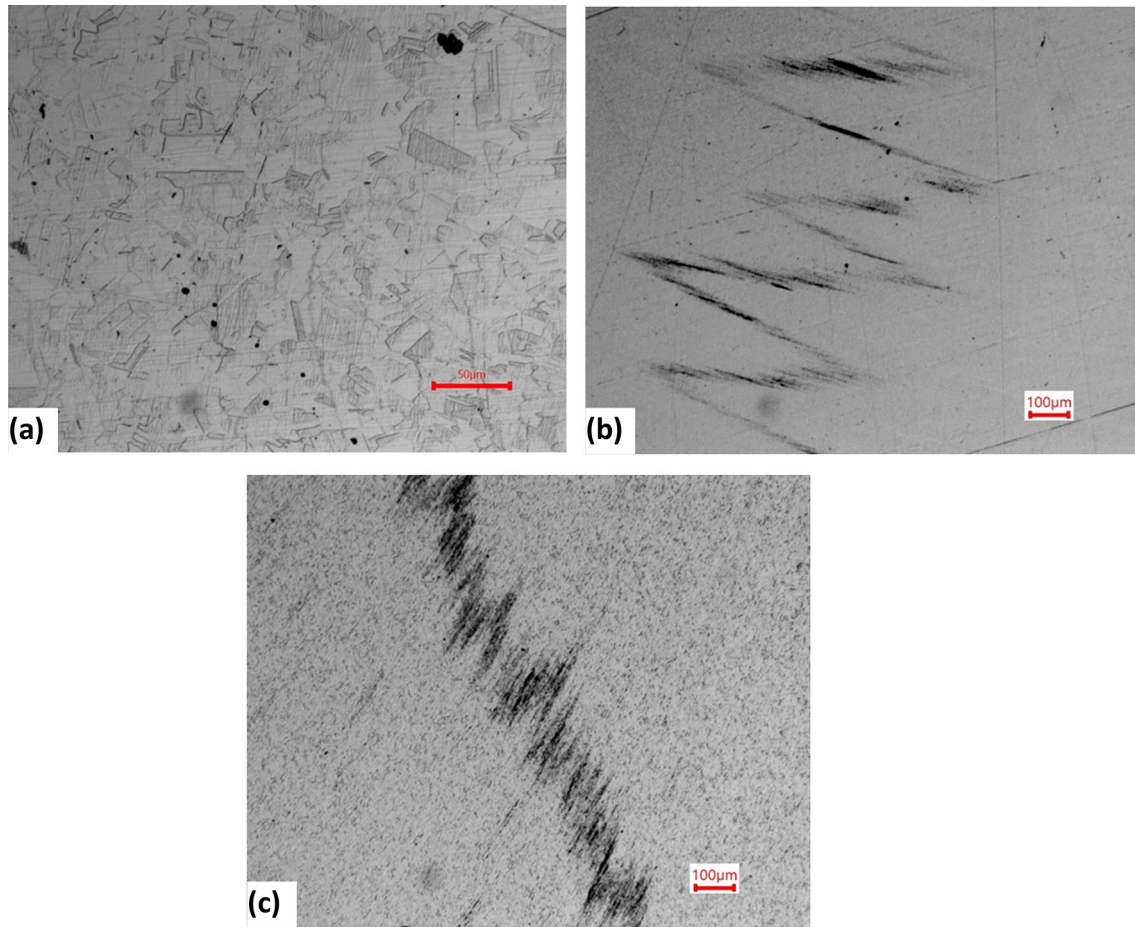
Fig. 11 Optical micrographs of specimens after conditioned at 0 $V_{Ag/AgCl}$ in 3.5% NaCl solution at room temperature. **a** Base metal, **b** stirred zone (SZ) under 725 °C isothermal condition, and **c** SZ at 825 °C. The samples were slightly etched to reveal the grain boundaries

4 Discussion

The experimental results discussed above indicate that overall corrosion resistance of the FSW specimens has significantly reduced compared to that of the base metal 304L SS. The polarization resistance (R_p) values obtained from both linear polarization and electrochemical impedance spectroscopy is a strong indicator of the base metal being more corrosion resistance than the other two samples. Grain size is one of the most important microstructural features that affects the corrosion properties in stainless steels. Grain refinement in 304L-type austenitic stainless steel was found to improve corrosion resistance in many studies [7, 44–47]. Sabooni et al. observed that the grain refinement did not affect the corrosion potential (E_{corr}) of 304L SS in 3.5% NaCl solution, but the corrosion rate (i_{corr}) and passive current density (i_{pass}) were significantly reduced and Rp increased with the smaller grain size [44]. A widely posited theory behind the enhanced corrosion resistance with the grain refinement is that increased grain boundary area with the smaller grain size promotes a better diffusion passage for the chromium to the formation of chromium-rich passive film on the surface. Contrary to the findings of the improved corrosion resistance on grain refinement in 304L SS, we have observed that the smaller grain size samples, both SZ-725 °C and SZ-825 °C (1–4 μm), showed a lower corrosion resistance (R_p of 3–7 kohm) compared to the coarse-grained (~ 44 μm) base metal (R_p ~ 16 kohm). The factors such as grain boundary character [8, 48], the presence of delta ferrite in austenitic stainless steel [49, 50], and residual stress [51, 52] which result from different thermomechanical routes during processing stainless steel are widely considered to control the corrosion resistance. Singh et al. observed that below a critical grain size (~ 16 μm), the grain boundary structure did not play any significant role in improving the corrosion resistance [53]. Therefore, the lower polarization resistance (R_p) value in fine-grained SZ-725 °C and SZ-825 °C samples could be attributed to the attack on the lazy-S
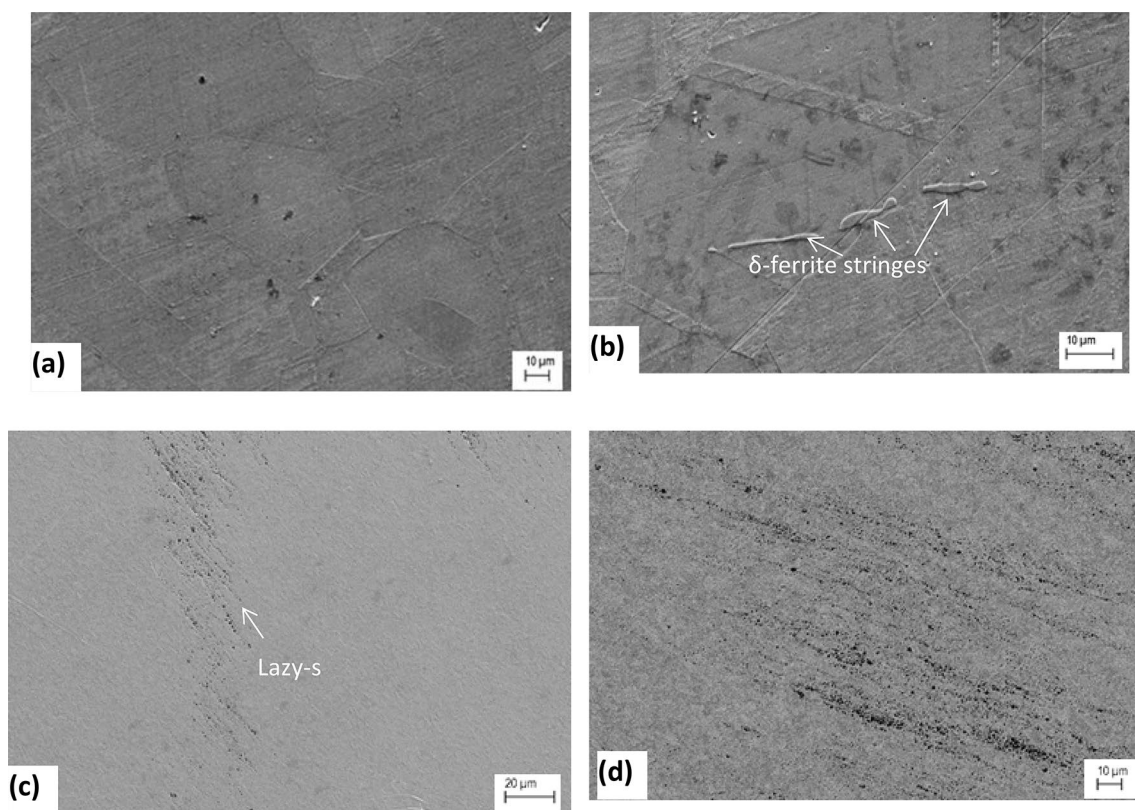
Fig. 12 SEM micrographs of specimens after conditioned at 0 $V_{Ag/AgCl}$ in 3.5% NaCl solution at room temperature. **a** Base metal, **b** base metal showing no pitting at delta ferrite stringes or ferrite–austenite interfaces, **c** preferential attack on the lazy-S region of the SZ at 825 °C, and **d** higher magnification of the lazy-S region shown in figure (**c**). The samples were slightly etched to reveal the grain boundaries

zone. A comparison between two different grain sizes, 15 µm and 38 µm, showed that the coarser grain size had a higher pitting resistance [7]. In the same study, it was observed that the corrosion potential was not affected by the grain size. Similar observation was made by Atapour et. al, who reported that the ultrafine-grained 304L SS (500 nm grain size) had much higher pitting resistance than that of the larger grain size (1–12 µm) ones, but the grain size reduction had a negligible effect on the corrosion potential [54]. A statistical method was employed by Aghug and the coworkers [55] in order to investigate the effect of grain size on the pitting resistance in 304L SS (5–28 µm) in 3.5% NaCl solution. They reported that the grain size had no effect on the pitting potential, but the grain refinement reduced the frequency of metastable pit formation. However, the smaller grain size increased the kinetics of metastable pit dissolution and the probability of the metastable pits to grow into a stable pit. Our study shows that the specimens with the smallest (SZ-725 °C) have the most noble pitting or breakdown potential (E_b), but the SZ-825 °C which has a relatively fine grain size (~4 µm) shows the most active

pitting potential, whereas the coarse-grained base metal (~50 µm) has an intermediate E_b value. Therefore, general and pitting corrosion resistance of the austenitic stainless steels cannot be controlled by just controlling the grain size. The grain boundary structures such as low-angle grain boundaries and special grain boundaries (coincidence site lattices) are considered to improve the general and pitting corrosion resistance of the austenitic stainless steels. The presence of Σ3 grain boundaries in the microstructure of austenitic stainless steels was considered to enhance the pitting resistance [56]. These grain boundaries are known as special grain boundaries with the low interfacial energies and reported to inhibit the pitting corrosion in other alloys as well [57]. It was shown that the 304 SS with high fraction of Σ3 grain boundaries and lower fraction of random high-angle grain boundaries (RHAGB) exhibited a superior pitting resistance to the 304 samples having lower Σ3 grain boundary fraction [7]. The pits formed preferentially on the RHAGB. Our results show pit formation on the grain interior for the base metal. The special grain boundaries not only improve the pitting resistance but also the intergranular and
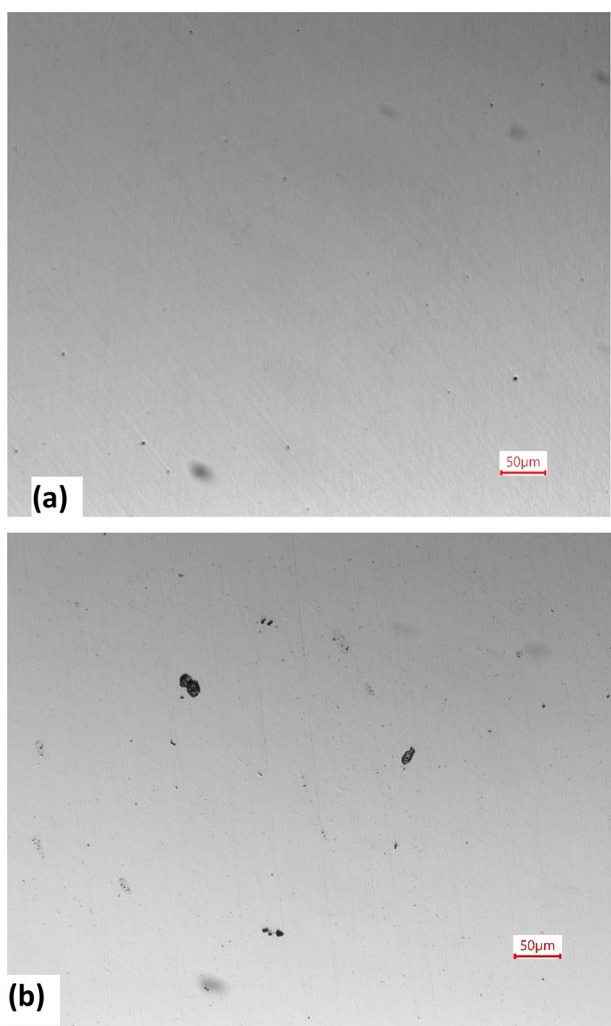
Fig. 13 Optical micrographs of SZ-825 °C specimen before and after potentiostatic conditioning at 0 $V_{Ag/AgCl}$ in 3.5% NaCl solution at room temperature. **a** Before testing, and **b** after pit growth

general corrosion in the austenitic stainless steels [58, 59]. Our result shows that the Σ3 grain boundary fraction has significantly reduced to 1–1.5% in the SZ-725 °C and SZ-825 °C samples from the 48% in the 304L base metal. In line with the idea discussed before, it can be concluded that the lower Σ3 grain boundary fraction detrimentally affected the corrosion resistance properties of SZ-725 °C and SZ-825 °C samples. Along with the lower Σ3 grain boundary fraction, the presence of the lazy-S regions further lowered the corrosion resistance in those samples. On the other hand, the FSWed specimens had a high fraction of low-angle grain boundaries that counteracted the detrimental effect of the lazy-S zones. As discussed in the earlier section, the linear array of dislocations that constitute low-angle boundaries could act as misorientation dislocations at the metal/oxide interface and promote formation of oxide without stressing the

substrate. Therefore, low-angle boundaries will be helpful for formation of stress-free passive films that will be more stable and enhance both pitting and stress corrosion cracking resistance.

5 Conclusions

Friction stir welding was carried out on 304L coupons with a simulated crack at two different tool temperatures such as 725 and 825 °C. Corrosion behavior of the friction stir repair-welded specimens of 304L SS was evaluated in the 3.5% NaCl solution and compared with the base metal by carrying out cyclic polarization, chronoamperometry, and electrochemical impedance spectroscopy. Based on the results, the following conclusions could be drawn:

The base metal of 304L SS had a mean grain size of 47 ± 16 μm. The grain size decreased to 2.4 ± 0.9 and 4.2 ± 1.4 μm upon friction stirring at 725 and 825 °C respectively. The base metal had a high fraction (~50%) of special grain boundaries such as Σ3 and Σ9. The friction stirring significantly reduced the special boundaries (< 10%), but increased fraction of low-angle grain boundaries from 25 to 37–43%. Furthermore, a preformed oxide layer that was present on the artificial crack surfaces was broken during the friction stirring and agglomerated as a spiral defect structure called 'lazy-S' due to its S shape.

These complex changes in the grain size and grain boundary character and the presence of the lazy-S defect structure after friction stirring negatively affected the pitting resistance of the specimens.

The FSW specimens showed lower polarization resistance and lower transpassive potential than those of the base metal specimens. However, the pitting protection potentials of the FSW specimens were higher than that of the base metal.

The pitting behavior of the FSW specimens was influenced more by the preferential attack on the lazy-S region than by passive film breakdown.

The flat band potentials of the passive film formed on the FSW specimens were more positive than that of base metal specimen which could lead to sluggish water or hydrogen reduction reaction as a cathodic reaction for the overall corrosion process. The charge carrier density of passive film formed on the FSW specimens was higher than that of the base metal.

The higher fraction of low-angle grain boundaries present in the FSW specimens could supply more number of misorientation dislocations at the metal/film interface which could form anion vacancies by a climb process leading to the formation of oxide at these locations without stressing the substrate. Therefore, low-angle boundaries will be helpful for formation of stress-free passive films

that will be more stable and enhance both pitting and stress corrosion cracking resistance.

Compliance with ethical standards

Conflict of interest The authors declare that they have no conflict of interest.

References

1. Hackel L, Rankin J, Walter M, Dane CB, Neuman W, Oneid P, Thomas G, Bidrawn F (2019) Preventing stress corrosion cracking of spent nuclear fuel dry storage canisters. Proced Struct Integr 19:346–361

2. Mayuzumi M, Tani J, Arai T (2008) Chloride induced stress corrosion cracking of candidate canister materials for dry storage of spent fuel. Nucl Eng Des 238(5):1227–1232

3. Li J, Liu YY (2016) Thermal modeling of a vertical dry storage cask for used nuclear fuel. Nucl Eng Des 301:74–88

4. Xie Y, Zhang J (2015) Chloride-induced stress corrosion cracking of used nuclear fuel welded stainless steel canisters: a review. J Nucl Mater 466:85–93

5. Bryan CR (2018) Research into Stress Corrosion Cracking of Spent Nuclear Fuel Dry Storage Canisters (No. SAND2018-5875C). Sandia National Lab (SNL-NM), Albuquerque

6. Asaduzzaman MD, Mohammad CM, Mayeedul I (2011) Effects of concentration of sodium chloride solution on the pitting corrosion behavior of AISI 304L austenitic stainless steel. Chem Indus Chem Eng Q 17(4):477–483

7. Pradhan SK, Bhuyan P, Mandal S (2019) Influence of the individual microstructural features on pitting corrosion in type 304 austenitic stainless steel. Corros Sci 158:108091

8. Meng G, Li Y, Shao Y, Zhang T, Wang Y, Wang F, Cheng X, Dong C, Li X (2016) Effect of microstructures on corrosion behavior of nickel coatings: (II) competitive effect of grain size and twins density on corrosion behavior. J Mater Sci Technol 32:465–469

9. Tokuda S, Muto I, Sugawara Y, Hara N (2020) Pit initiation on sensitized Type 304 stainless steel under applied stress: correlation of stress, Cr-depletion, and inclusion dissolution. Corros Sci 167:108506

10. Duan Z, Man C, Dong C, Cui Z, Kong D, Wang X (2020) Pitting behavior of SLM 316L stainless steel exposed to chloride environments with different aggressiveness: Pitting mechanism induced by gas pores. Corros Sci 167:108520

11. Ezuber H, AlShater A, Nisar S, Gonsalvez A, Aslam S (2018) Effect of surface finish on the pitting corrosion behavior of sensitized AISI 304 austenitic stainless steel alloys in 3.5% NaCl solutions. Surf Eng Appl Electrochem 54:73–80. https://doi.org/10.3103/S1068375518010039

12. Tang W, Chatzidakis S, Miller R, Chen J, Kyle D, Scaglione J, Schrad C (2019) Welding process development for spent nuclear fuel canister repair. In ASME 2019 pressure vessels & piping conference. American society of mechanical engineers digital collection

13. Ross KA, Alabi M (2019) Update on investigations of viability of cold spray and FSW as a spent nuclear fuel dry storage canister mitigation tool (No. PNNL-29217). Pacific Northwest National Lab (PNNL), Richland

14. Gunter C, Miles MP, Liu FC, Nelson TW (2018) Solid state crack repair by friction stir processing in 304L stainless steel. J Mater Sci Technol 34(1):140–147

15. Hsu CH, Chen TC, Huang RT, Tsay LW (2017) Stress corrosion cracking susceptibility of 304L substrate and 308L weld metal exposed to a salt spray. Materials 10(2):187

16. Kumar SS, Murugan N, Ramachandran KK (2018) Microstructure and mechanical properties of friction stir welded AISI 316L austenitic stainless steel joints. J Mater Process Technol 254:79–90

17. Lü AQ, Zhang Y, Li Y, Liu G, Zang QH, Liu CM (2006) Effect of nanocrystalline and twin boundaries on corrosion behavior of 316L stainless steel using SMAT. Acta Metall Sin (Engl Lett) 19:183–189

18. Ralston KD, Birbilis N (2010) Effect of grain size on corrosion: a review. Corrosion 66:075005–075013

19. Roy I, Yang HW, Dinh L, Lund I, Earthman JC, Mohamed FA (2008) Possible origin of superior corrosion resistance for electrodeposited nanocrystalline Ni. Scripta Mater 59:305–308

20. Chan LH, Weiland H, Cheong S, Rohrer GS, Rollett AD (2008) The correlation between grain boundary character and intergranular corrosion susceptibility of 2124 aluminum alloy. In: Rollett AD (ed) Applications of texture analysis. Wiley, Hoboken, pp 261–267

21. Sarlaka H, Atapoura M, Esmailzadeh M (2015) Corrosion behavior of friction stir welded lean duplex stainless steel. Mater Des 66A:209–216

22. Li HB, Jiang ZH, Feng H, Zhang SC, Li L, Han PD, Misra RDK, Li JZ (2015) Microstructure, mechanical and corrosion properties of friction stir welded high nitrogen nickel-free austenitic stainless steel. Mater Des 84:291–299

23. Zhang H, Xue P, Wang D, Wu LH, Ni DR, Xiao BL, Ma ZY (2019) Effect of heat-input on pitting corrosion behavior of friction stir welded high nitrogen stainless steel. J Mater Sci Technol 35:1278–1283

24. Sato YS, Harayama N, Kokawa H, Inoue H, Tadokoro Y, Tsuge S (2009) Evaluation of microstructure and properties in friction stir welded superaustenitic stainless steel. Sci Technol Weld Joining 14(3):202–209

25. Zhang H, Wang D, Xue P, Wu LH, Ni DR, Xiao BL, Ma ZY (2019) Microstructure and corrosion resistance of friction stir welded high nitrogen stainless steel joint. Corrosion 75(7):790–798

26. Xu S, Deng X (2008) A study of texture patterns in friction stir welds. Acta Mater 56:1326–1341. https://doi.org/10.1016/j.actamat.2007.11.016

27. Tongne A, Desrayaud C, Jahazi M, Feulvarch E (2017) On material flow in friction stir welded Al alloys. J Mater Process Technol 239:284–296. https://doi.org/10.1016/j.jmatprotec.2016.08.030

28. Krishnan KS (2002) On the formation of onion rings in friction stir welds. Mater Sci Eng A 327:246–251. https://doi.org/10.1016/S0921-5093(01)01474-5

29. Kumar KSVK, Kailas SV (2008) The role of friction stir welding tool on material flow and weld formation. Mater Sci Eng A 485:367–374. https://doi.org/10.1016/j.msea.2007.08.013

30. Palanivel R, Mathews PK, Murugan N, Dinaharan I (2012) Effect of tool rotational speed and pin profile on microstructure and tensile strength of dissimilar friction stir welded AA5083-H111 and AA6351-T6 aluminum alloys. Mater Des 40:7–16. https://doi.org/10.1016/j.matdes.2012.03.027

31. Sato YS, Nelson TW, Sterling CJ (2005) Recrystallization in type 304L stainless steel during friction stirring. Acta Mater 53:637–645. https://doi.org/10.1016/j.actamat.2004.10.017

32. Cui HB, Xie GM, Luo ZA, Ma J, Wang GD, Misra RDK (2016) Microstructural evolution and mechanical properties of the stir zone

in friction stir processed AISI201 stainless steel. Mater Des 106:463–475. https://doi.org/10.1016/j.matdes.2016.05.106

33. Dieter GE (1986) Mechanical metallurgy, 3rd edn. McGraw-Hill Book Company, New York, pp 193–197

34. Heakal FET, Hefny MM, El-Tawab AA (2010) Electrochemical behavior of 304L stainless steel in high saline and sulphate solutions containing alga Dunaliella Salina and β-carotene. J Alloy Compd 491(1–2):636–642

35. Ma Y, Guo ZL, Qiao JC, Bai HT (2019) Pitting corrosion failure analysis of a produced oil/water fluid pipeline. Mater Sci Forum 953:39–44 (**Trans Tech Publications**)

36. Chang BY, Park SM (2010) Electrochemical impedance spectroscopy. Annu Rev Anal Chem 3:207–229

37. B Pieraggi, RA Rapp, JOURNAL DE PHYSIQUE IV, Colloque C9, supplement au Journal de Physique III, Volume 3, 1993, 275 - 280

38. Papamarkou T, Guy H, Kroencke B, Miller J, Robinette P, Schultz D, Hinkle J, Pullum L, Schuman C, Renshaw J, Chatzidakis, S (2020) Automated detection of pitting and stress corrosion cracks in used nuclear fuel dry storage canisters using residual neural networks. arXiv preprint arXiv: 2003.03241

39. Jones DA (1996) Principles and prevention of corrosion, 2nd edn. Prentice Hall, Upper Saddle River

40. Salih SM, Shakir IK, Al-Sammarraie AMA (2017) Comparison of aggressiveness behavior of chloride and iodide solutions on 304 and 304L stainless steel alloys. Mater Sci Appl 8(12):889–898

41. Macdonald DD (1992) The point defect model for the passive state. J Electrochem Soc 139(12):3434–3449

42. Sato N (1989) Toward a more fundamental understanding of corrosion processes. Corrosion (NACE) 45:354–368

43. Korjenic A, Raja KS (2019) Electrochemical stability of fluorine doped tin oxide (FTO) coating at different pH conditions. J Electrochem Soc 166(6):C169–C184

44. Sabooni S, Rashtchi H, Eslami A, Karimzadeh F, Enayati MH, Raeissi K, Ngan AHW, Imani RF (2017) Dependence of corrosion properties of AISI 304L stainless steel on the austenite grain size. Int J Mater Res 108(7):552–559

45. Olugbade T, Lu J (2019) Enhanced corrosion properties of nanostructured 316 stainless steel in 0.6 M NaCl solution. J Bio Tribo Corros 5(2):38

46. Di Schino A, Kenny JM (2002) Effects of the grain size on the corrosion behavior of refined AISI 304 austenitic stainless steels. J Mater Sci Lett 21(20):1631–1634

47. Rifai M, Miyamoto H, Fujiwara H (2015) Effects of strain energy and grain size on corrosion resistance of ultrafine grained Fe-20% Cr steels with extremely low C and N fabricated by ECAP. Int J Corros 2015:1–9

48. Qi J, Huang B, Wang Z, Ding H, Xi J, Fu W (2017) Dependence of corrosion resistance on grain boundary characteristics in a high nitrogen CrMn austenitic stainless steel. J Mater Sci Technol 33:1621–1628

49. Rumiche F, Juarez C, Nuñez R (2019) Macro and micro scale corrosion of 316L stainless steel: a case study of a hole plate. J Fail Anal Prev 19(5):1218–1224

50. Subramanian GO, Hong S, Lee HJ, Kong BS, Lee KS, Byun TS, Jang C (2019) Electrochemical characteristics of delta ferrite in thermally aged austenitic stainless steel weld. In proceedings of the 18th international conference on environmental degradation of materials in nuclear power systems–water reactors (pp. 1869–1877). Springer, Cham

51. Feng X, Lu X, Zuo Y, Zhuang N, Chen D (2016) The effect of deformation on metastable pitting of 304 stainless steel in chloride contaminated concrete pore solution. Corros Sci 103:223–229

52. Phadnis SV, Satpati AK, Muthe KP, Vyas JC, Sundaresan RI (2003) Comparison of rolled and heat treated SS304 in chloride solution using electrochemical and XPS techniques. Corros Sci 45:2467–2483

53. Singh R, Chowdhury SG, Chattoraj I (2008) Modification of sensitization resistance of AISI 304L stainless steel through changes in grain size and grain boundary character distributions. Metall Mater Trans A 39(10):2504–2512

54. Atapour M, Dana MM, Ashrafizadeh F (2015) A corrosion study of grain-refined 304L stainless steels produced by the martensitic process. Int J Iron Steel Soc Iran 12(2):30–38

55. Aghuy AA, Zakeri M, Moayed MH, Mazinani M (2015) Effect of grain size on pitting corrosion of 304L austenitic stainless steel. Corros Sci 94:368–376

56. Arafin MA, Szpunar JA (2009) A new understanding of intergranular stress corrosion cracking resistance of pipeline steel through grain boundary character and crystallographic texture studies. Corros Sci 51(1):119–128

57. Bai Q, Zhao Q, Xia S, Wang B, Zhou B, Su C (2017) Evolution of grain boundary character distributions in alloy 825 tubes during high temperature annealing: is grain boundary engineering achieved through recrystallization or grain growth? Mater Charact 123:178–188

58. Shimada M, Kokawa H, Wang ZJ, Sato YS, Karibe I (2002) Optimization of grain boundary character distribution for intergranular corrosion resistant 304 stainless steel by twin-induced grain boundary engineering. Acta Mater 50(9):2331–2341

59. Wasnik DN, Kain V, Samajdar I, Verlinden B, De PK (2004) Effects of overall grain boundary nature on localized corrosion in austenitic stainless steels. Mater Sci Forum 467:813–818 (**Trans Tech Publications Ltd**)